Regional Moment Tensors of the 2009 L'Aquila Earthquake Sequence

3 authors:

Robert Herrmann
Saint Louis University
154 PUBLICATIONS   **2,896** CITATIONS

SEE PROFILE

Irene Munafò
National Institute of Geophysics and Volcanology
9 PUBLICATIONS   **260** CITATIONS

SEE PROFILE

Luca Malagnini
National Institute of Geophysics and Volcanology
115 PUBLICATIONS   **2,544** CITATIONS

SEE PROFILE

Some of the authors of this publication are also working on these related projects:

Project   Western United States Velocity Structure View project

Ⓔ

Regional Moment Tensors of the 2009 L'Aquila Earthquake Sequence

by Robert B. Herrmann, Luca Malagnini, and Irene Munafò

Abstract   Broadband waveform inversion of ground velocities in the 0.02–0.10 Hz frequency band is successfully applied to 181 earthquakes with $M_L \geq 3$ of the April 2009 L'Aquila, Italy, earthquake sequence. This was made possible by the development of a new regional crustal velocity model constrained by deep crustal profiles, surface-wave dispersion and teleseismic P-wave receiver functions, and tested through waveform fit. Although all earthquakes exhibit normal faulting, with the fault plane dipping southwest at about 55° for the majority of events, a subset of events had much shallower dips. The issue of confidence in the derived parameters was investigated by applying the same inversion procedure by two groups who subjectively selected different traces for inversion. The unexpected difficulty in modeling the regional broadband waveforms of the mainshock as a point source was investigated through an extensive finite-fault modeling of broadband velocity and accelerometer data, which placed the location of major moment release up-dip and about 4–7 s after the initial first-arrival hypocentral parameters.

Online Material: Table of moment tensors.

Introduction

On 6 April 2009 at 01:32:39 UTC, an M_L 5.8 earthquake occurred in Regione Abruzzo (central Italy). The initial hypocentral coordinates were 42.33° N, 13.33° E, and depth of 8.8 km (from Istituto Nazionale di Geofisica e Vulcanologia [INGV]; see Data and Resources section). The event ruptured up-dip in the southeast direction (Cirella *et al.*, 2009), causing extensive damage in the city of L'Aquila and in many villages of the region. A total of 308 casualties and 1500 injuries resulted from the collapse of buildings that could not withstand the strong ground shaking, and 64,812 people were displaced from their homes (Akinci and Malagnini, 2009).

The rupture occurred on the Paganica fault (Walters *et al.*, 2009), a poorly known structure that is now being extensively investigated (see also Emergeo Working Group, 2009). Anzidei *et al.* (2009) observed a maximum surface displacement of 10 ± 0.5 cm horizontally and -16 ± 2 cm vertically, consistent with a fault plane dipping $55° \pm 2°$. Surface displacement is located on the projection of the fault plane, indicated by the spatial distribution of aftershocks (Chiaraluce *et al.*, 2010). The best fit to the geodetic data by Anzidei *et al.* (2009) was achieved with a rupture surface of 13×16 km² and an estimated average slip of 49 ± 3 cm, corresponding to an M_w 6.3 earthquake.

The strong ground motion was severe in some locations, with recorded peak accelerations up to $\sim 1g$, clearly indicating (Akinci *et al.*, 2010) the southeastward directivity of the rupture found by Cirella *et al.* (2009), who jointly inverted strong-motion and GPS data (Anzidei *et al.*, 2009) for rupture properties. Atzori *et al.* (2009) inverted the differential synthetic aperture radar interferometry (DInSAR; Massonnet *et al.*, 1993) coseismic displacement for the slip distribution on the Paganica fault.

The mainshock was preceded by a swarmlike activity that started a year earlier. For this study of all the events with $M_L \geq 3$, our data set starts on 1 October 2008 at 22:47:37 UTC, when an event of M_L 3.1 (M_w 3.20, this study) was located at 42.59° N and 13.29° E (see the Data and Resources section). The swarmlike activity lasted through 6 April, when the mainshock hit. Seven events with M_L values between 3.0 and 4.0 occurred in the week preceding the main earthquake, four of them on 30 March 2009, one on 3 April, and the remaining two on 5 April 2009. The entire swarm, and its abrupt acceleration in particular, may be interpreted now *a posteriori* as a precursor to the imminent occurrence of the main event. Unfortunately, it was not possible to foresee the main event before its occurrence. Four large aftershocks (M_w values 4.75, 4.81, 4.90, and 5.42, this study) occurred close to the city of L'Aquila on 7 April 2009 within 36 hr of the mainshock, while another large aftershock (M_w 5.22, this study) occurred to the north of the city on 9 April 2009.

The occurrence of a destructive event in the vicinity of L'Aquila is not surprising, because three large events (intensity X) affected L'Aquila in the last 650 yr (1349, 1461, and 1703; Stucchi *et al.*, 2007). In recent years, some seismic sequences with an $M_L \leq 4.0$ occurred in the area (De Luca

et al., 2000; Boncio *et al.*, 2004; Chiarabba *et al.*, 2005; Pace *et al.*, 2006). Deformation rates in the area were also precisely known well before the main event of 6 April 2009; the area along the mountain belt is deforming in extension (2–3 mm/yr; Hunstad *et al.*, 2003) within a 50-km-wide area containing the highest topographic features (Selvaggi *et al.*, 1997). The northeast-trending orientation of the extension is consistent with focal mechanisms (Montone *et al.*, 2004; Bagh *et al.*, 2007), borehole breakouts (Mariucci *et al.*, 1999), and geological data (Westaway, 1992; Lavecchia *et al.*, 1994). Chiarabba *et al.* (2005) reviewed previous studies and stated that the seismotectonics along the Apennines are controlled by the north-eastward retreat of the Adria subducting slab and showed that the seismogenic layer in the region ranges between 6 and 16 km, in good agreement with the depths obtained from the waveform inversions of this study. More importantly, a number of recent studies, supported through grants of the Italian Protezione Civile (e.g., Pace *et al.*, 2006; Akinci *et al.*, 2009), estimated the seismic hazard for the central Apennines and highlighted the elevated hazard in the area surrounding L'Aquila.

The study by Bagh *et al.* (2007) investigated the background seismicity in the Abruzzo region by relocating a large number of events recorded in the previous 20 yr by different permanent and temporary seismic networks. They observed that the background seismicity was generally sparse with a few dense clusters due to small sequences (a few of them near L'Aquila). The seismic activity in the central Apennines, as shown in Bagh *et al.* (2007), is distributed in the upper 15 km of the crust and consists predominantly of normal faulting with strike parallel to the mountain belt (55% of the cases), with some pure strike-slip faulting (27% of the cases), and with the remainder having transtensional mechanisms. Bagh *et al.* (2007) stated that the major active structures in the Apennines are locked normal faults, which when activated, cause secondary strike-slip structures that redistribute the perturbed stress field.

Recently INGV has upgraded the national seismic network (Amato and Mele, 2008; Michelini *et al.*, 2008) and provided access to event recordings through the Italian Instrumental and Parametric Data-Base (ISIDe, see the Data and Resources section). ISIDe provides access to the catalog of located earthquakes and links to the waveforms with responses. Because events are quickly posted, the event data can be quickly downloaded and processed for moment-tensor inversion. This study developed processing procedures to study the larger events of the sequence, derived a local velocity model to be used for waveform inversion, and determined that moment-tensor inversions could easily be obtained for earthquakes as small as M_L 3.0. Figure 1 shows the ISIDe location for all events with $M_L > 2$ in the vicinity of the 6 April mainshock. The figure also highlights the locations of earthquakes with $M_L \geq 3$ that are the subject of this paper.

We waveform-modeled 181 events in the 0.02–0.10 Hz frequency band with $M_L \geq 3$ that occurred in the L'Aquila region between 1 October 2008 and 31 January 2010. The
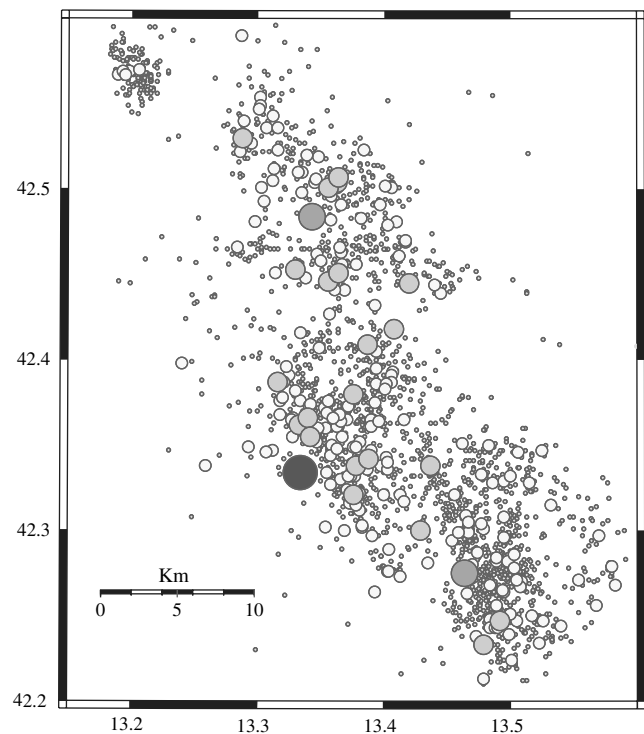

Figure 1.   INGV catalog locations plotted to the nearest 0.1° for the time period 1 October 2008 through 3 February 2010 showing the locations of earthquakes, binned in the magnitude ranges 2.0–2.9, 3.0–3.9, 4.0–4.9, 5.0–5.4, and 5.5–6.0. The symbol size is proportional to the magnitude bin. The numbers of earthquakes within each bin are 21,239, 233, 25, 3, and 1, respectively. This study focuses on earthquakes with $M_L \geq 3.0$.

inversions for the moment-tensor solutions were performed after we developed a regional velocity model based on profiles shown in Di Luzio *et al.* (2009). Their figure 5 shows a crustal geologic section taken along the Crosta Profonda (CROP) profile 11, from the Adriatic foreland on the east to the Fucino basin on the west. The CROP seismic profiles were performed in the 1980s in order to investigate the deep crust across the Apennines, and their data were recently released (Scrocca *et al.*, 2003). The purpose of our paper is to document the inversion procedure, including the development of a regional crustal velocity model, to evaluate the capabilities of the broadband network and to understand the complex process of this earthquake sequence. We accomplish these objectives by defining the velocity model, by presenting the moment-tensor solutions, and then by examining our difficulties in determining the source parameters of the main event of the sequence.

Velocity Model

As part of an effort for implementing routine regional moment-tensor inversion in routine processing at the United States Geological Survey (USGS) National Earthquake Information Center, R. B. Herrmann (unpublished manuscript, 2010) documented a procedure for systematic

moment-tensor inversion of continental earthquakes in the United States and Canada through a rapid grid-search procedure (Herrmann and Ammon, 2002). Much has been learned from this effort, especially as catalog completeness was extended to magnitudes less than 4.0. Signal-to-noise limitations for small earthquakes can be overcome by focusing on higher frequency content of the signal, which in turn, requires velocity models capable of matching the detail observed at higher frequencies. The use of the appropriate regional velocity model is important not only to match the waveforms but also to define the moment magnitude of the earthquake because the theoretical amplitudes at high frequencies depend very strongly on the velocity model.

Our preliminary processing of the L'Aquila aftershocks used a model for tectonic North America (R. B. Herrmann, unpublished manuscript, 2010) for which we had a set of precomputed Green's functions. We quickly determined that we could perform regional moment-tensor inversions using the ISIDe data sets at local magnitudes of 4.0 and much lower because of the inherent high quality of the data sets and the large number of nearby broadband seismic stations. While performing quality control on the observed waveforms, we noted the presence of recognizable dispersed surface-wave trains, which suggested the application of the data processing and inversion tools of Herrmann and Ammon (2002) to define a specific velocity model for use in the study area.

We made group velocity measurements using multiple-filter analysis (Herrmann, 1973) on 80 vertical and transverse-component waveforms for six aftershocks to yield about 600 Rayleigh- and Love-wave dispersion measurements in the 4.4- to 28-s period range, being careful not to select the longer periods at short epicentral distances for which the dispersion was not yet well developed. The aftershocks and stations used for the group velocity study, Figure 2, sample the central Apennines, and thus any derived velocity model is appropriate for these paths or for a similar structural environment.

The starting model, given in Table A1 of the Appendix, was based on the work of Di Luzio *et al.* (2009) who interpreted the seismic data from a deep seismic reflection profile across the Appenines that passed near L'Aquila. The crustal model for their stations 7–8, near L'Aquila, was used to define the deeper crustal boundaries and *P*-wave velocities. The surface-wave inversion program, *surf96* (Herrmann and Ammon, 2002), was run with a smoothing constraint to find a simple model that matches the observations. To be consistent with the major structural boundaries in the work of Di Luzio *et al.* (2009), we applied stronger weighting to permit a basin boundary at a depth of 3 km and fixed the velocities of the half-space and deepest crustal layer in the model. We permitted the other crustal velocities, with emphasis on the upper crustal velocities, to change because the surface-waves are the dominant signal for the time-domain moment-tensor inversion and are, in turn, affected by upper crustal *S*-wave velocities. Moreover, the strong *P*-wave signal often
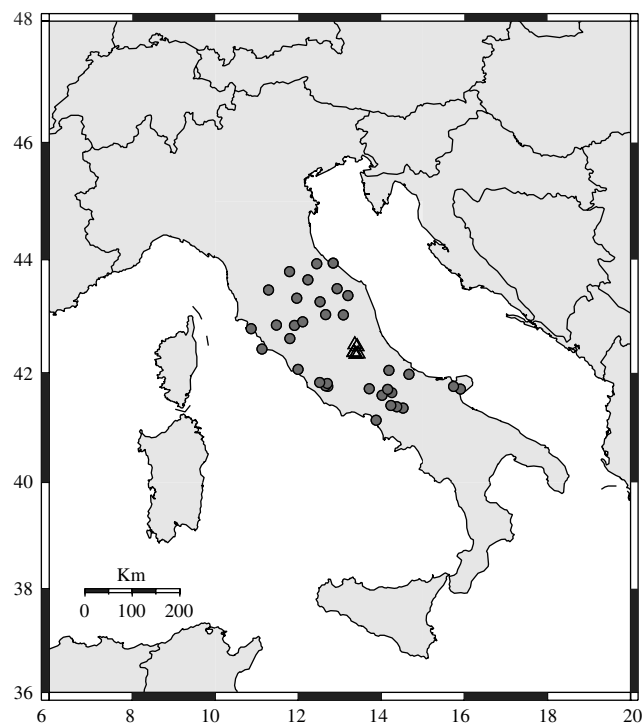

Figure 2. Map showing earthquakes (triangles) and stations (solid circles) used for the group velocity analysis to determine the regional velocity model. The dispersion paths sample the structure of central Italy for a source in the central Apennines.

observed out to 100 km also is controlled by the upper crustal velocities. The starting model has a low velocity in the midcrust because of the westward subduction beneath the Apennines (see Chiarabba *et al.*, 2005). The resulting surface wave–based velocity model given in Table A1 of the Appendix, named central Italian Apennines (CIA), is thus constructed to be consistent with earlier studies as well as the measured dispersion.

Being aware that fundamental-mode surface-wave dispersion data cannot resolve sharp discontinuities in the velocity model, we also assembled a representative data set of radial-component *P*-wave receiver functions for the MedNet station AQU at L'Aquila for nine earthquakes using the low-pass filter parameter $\alpha = 1.0$ with the time-domain iterative deconvolution technique of Ligorria and Ammon (1999). The station AQU was selected for analysis because it lies within the region for which the velocity model is required and because waveforms were easily available from data archives. Because many crustal studies make use of receiver functions, neglecting their use would call into question the value of a velocity model based only on surface waves. These receiver functions were inverted together with the dispersion data using the program *joint96* (Herrmann and Ammon, 2002) to yield the joint surface-wave dispersion-receiver function model given in Table A1 of the Appendix as Appennino Centrale d'Italia (ACI). Because our objective was to augment the CIA model determined using *surf96*, the CIA model was used as the starting model, with the difference

that we subdivided many layers to be able to fit the finer features of the receiver functions. We did not permit the half-space velocity to change and again placed more emphasis on the change in layer velocities in the upper 10 km because the ringing character of the receiver functions is strongly affected by the presence of low-velocity sedimentary basins.

Figure 3 compares our observed dispersion with the predictions of the CIA, ACI, BAGH (named after S. Bagh [Bagh *et al.*, 2007]), and time domain moment tensor (TDMT; Scognamiglio *et al.*, 2009) models. The scatter in the observed dispersion is related to location and origin time error, the effect of 3D structure, and biases in the multiple-filter analysis determinations. However, the mean is assumed stable enough to define the dispersed shape of the observed waveforms. The upper 1.5 km of the Bagh *et al.* (2007) model was modified to have lower velocities in accordance with borehole information in the L'Aquila region (L. Scognamiglio, personal commun., 2009). The TDMT model is used for the INGV regional moment-tensor determination. The TDMT model cannot match the observed dispersion, because of the thick low-velocity layers near the surface that give rise to the very low fundamental-mode group velocities at shorter periods. The BAGH model is better at shorter periods, but our *ad hoc* extension of the model to depths greater than the 20 km of the Bagh *et al.* (2007) model was not adequate and demonstrates the need for defining the complete crustal model. Because both the CIA and ACI models were based on the inversion of the dispersion data, they fit the observed dispersion well.

Figure 4 shows the result of the joint inversion of the surface-wave dispersion and *P*-wave receiver functions at

AQU. The figure shows both the starting and final models for the inversion, CIA and ACI, respectively. Although the receiver-function fit is not perfect, the observed ringing fits at the beginning of the graph. For this station, the ringing due to the effect of the shallow velocity structure dominates any effect of deeper crustal structure beneath the MedNet station L'Aquila.

Figure 5 compares the four models. The low velocities of the upper 8 km of the TDMT are obvious, as is the assumed higher velocity lower crust of the BAGH model. The additional detail in the ACI model (solid gray line) compared with the simpler CIA model (solid black line) is required to model the observed long-duration ringing of the AQU receiver functions.

For use in source inversion, we initially computed Green's functions for both the CIA and ACI models and found they were similar when these were filtered in the 0.02–0.10 Hz band used for the source inversion, which is not surprising, because both fit the observed dispersion in the same way. For reasons of computational speed, we used the simpler CIA model to compute an extensive set of Green's functions for depths between 1 and 29 km in 1 km increments, and epicentral distances between 1 and 350 km at 1 km increments. A perfectly elastic model is used because the effect of reasonable *Q* values in modeling observations in the low-frequency band and at the short epicentral distances would be negligible.

Moment-Tensor Solutions

When we concluded that it was possible to determine source parameters for earthquakes with $M_L \geq 3$, we
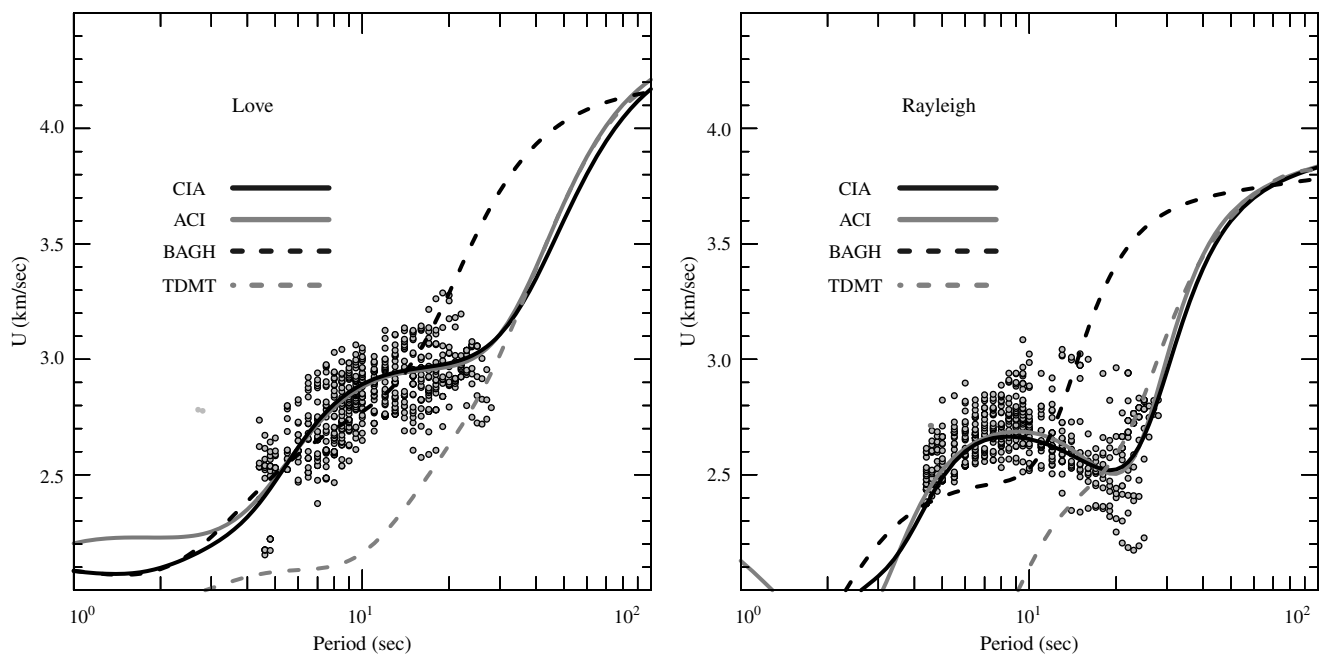

Figure 3. Comparison of observed (gray dots) and predicted (curves) Love- and Rayleigh-wave group velocity dispersion for different models: CIA, ACI, BAGH, and TDMT. The observed groups velocities were obtained for the stations and earthquakes shown in Figure 2.
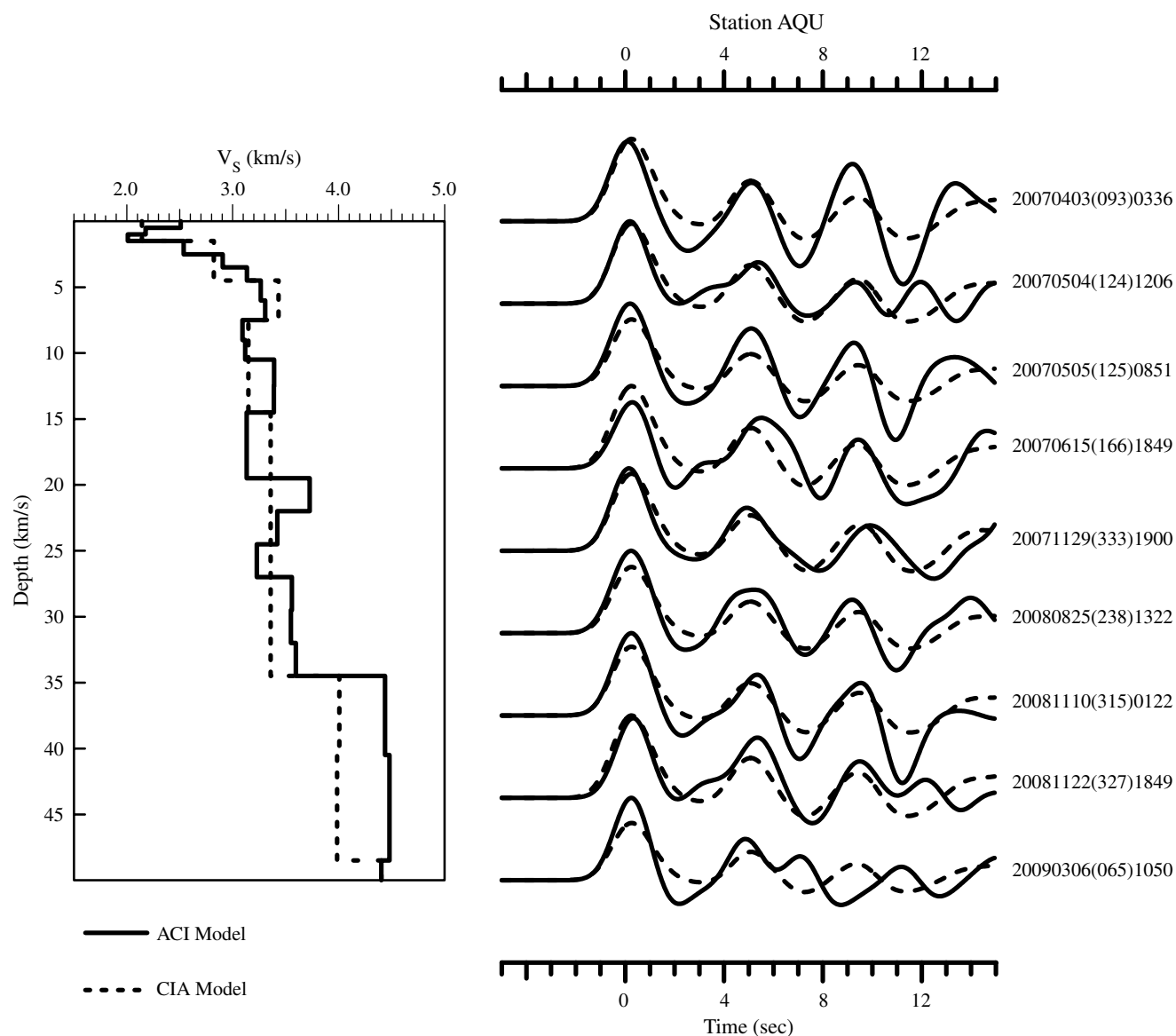
Figure 4. Left: comparison of the starting CIA and final ACI models for the joint inversion of surface-wave dispersion and receiver functions. Right: comparison of observed (solid) and ACI model predicted (dashed) *P*-wave receiver functions at the Mednet station AQU. The individual receiver functions are annotated on the right by event information.

developed bash shell scripts to ensure a uniform approach to the inversion and to reduce the need for manual intervention. The event location from ISIDe was used to initiate the processing. The ISIDe archive containing the waveforms and corresponding pole-zero files was unpacked. An initial quality control step (QC), applied to eliminate waveforms with data gaps or noisy signals, was followed by a second QC that examined the deconvolved ground-velocity waveforms in the 0.02–0.10 Hz band typically used for inversion. A final QC of the inversion results served to identify problematic waveforms, which were eliminated. (See the Data and Resources section for a web page presenting a record of all processing steps.) In spite of trans-Atlantic download times, we often

had a solution posted on the web page within 30 to 60 min of the event notification.

The grid search for source parameters uses filtered ground velocity as a data set to search for the best-fitting shear dislocation characterized by the strike and dip of the fault plane and the rake angle giving the direction of fault movement on the fault plane. For each source depth, a search is performed over all values of strike, dip, and rake angles at 10° increments, followed by a finer 5° search in a region ±20° about the crude best fit. The best fit is defined as the greatest reduction in weighted variance with each trace weighted as a function of epicentral distance in a manner that is proportional to distance out to 100 km and inversely
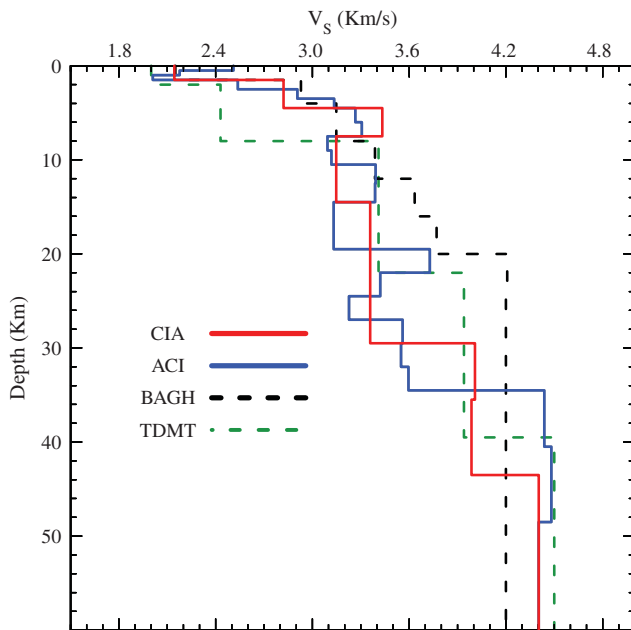
Figure 5.   Comparison of velocity models. The CIA model is used for source inversion.

proportional to distance beyond 100 km to overcome the dominance of large amplitudes and the effects of mislocation on azimuth at short distance and inadequacies in the velocity model at larger distances. The R. B. Herrmann (unpublished manuscript, 2010) grid-search algorithm permits a time shift to better align the waveforms to overcome mislocation and slight inadequacies of the Green's functions for the path to each station. We have found that the derived time shift is diagnostic of mislocation error and the need for velocity model improvement.

The determination of the passband for inversion is critical. We accomplish this by applying a three-pole causal high-pass Butterworth filter at the lower corner followed by a three-pole causal low-pass Butterworth filter at the upper corner. The corner frequencies were selected on the basis of the expected fundamental-mode surface-wave spectral shape, on avoiding instrumental and ground noise at low frequencies, microseism noise, and the consequence of using an imperfect crustal model at higher frequencies. The upper corner should also be adjusted to be lower than the corner frequency of the earthquake; the 0.02–0.10 Hz band was used for all earthquakes except for the mainshock, for which we used the 0.01–0.025 Hz frequency band. The choice of using ground velocity filtered in the 0.02–0.10 Hz frequency band was made to be able to analyze small earthquakes and to check on the appropriateness of the velocity model in as wide a bandwidth as possible.

Of the 235 earthquakes in the INGV catalog in the 2 September 2008 to 31 January 2010 time period with $M_L \geq$ 3 and greater, we were able to determine source parameters for 181 of these earthquakes. As an example of the proces-

sing, consider the event of 12 August 2009, 14:51:33 UTC. For this earthquake, we selected 23 vertical-component (Z), 7 radial-component (R), and 10 transverse-component (T) waveforms for inversion. Figure 6 shows the stations used in relation to the epicenter. The epicentral distances range from 18 to 146 km. Figure 7 plots the goodness of fit, the reduction in distance-weighted variance as a function of source depth, with the best mechanisms associated with each source depth; the best fit occurs at a depth of 7 km. Figure 8 overlays the filtered observed waveforms on top of those predicted for the best solution. There is an excellent fit between observed and predicted waveforms. More importantly, the time shifts, indicating the shift of the predicted (Fig. 8, dashed) with respect to the observed (Fig. 8, solid) traces, are typically on the order of 1 s, which indicates a consistency in the ISIDe source location and origin time (our relocation using the CIA model with our arrival time picks gave the same epicenter and origin time) as well as the applicability of the CIA velocity model. The increasingly negative time shifts for the Rayleigh-wave pulse on the Z component as distance increases indicates that the model could be about 3%–4% faster for the Rayleigh waves. The shapes of the observed and predicted signals match well.

To address the fundamental issue of the usefulness of this model, we ran the inversion in different frequency bands, with the results shown in Table 1. Although the goodness of fit depends on the frequency band used, the source parameters are quite similar. At the lowest frequency, the reduced fit parameter is due to long period noise. At the highest frequency, the effect of scattered waves degrades the fit.
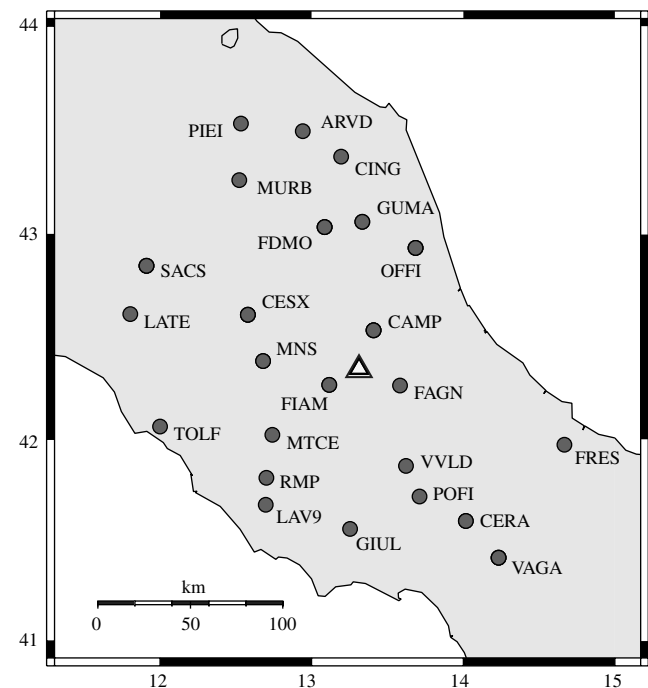

Figure 6.   Location of the earthquake and stations used to analyze the earthquake of 12 August 2009, 14:51:33.
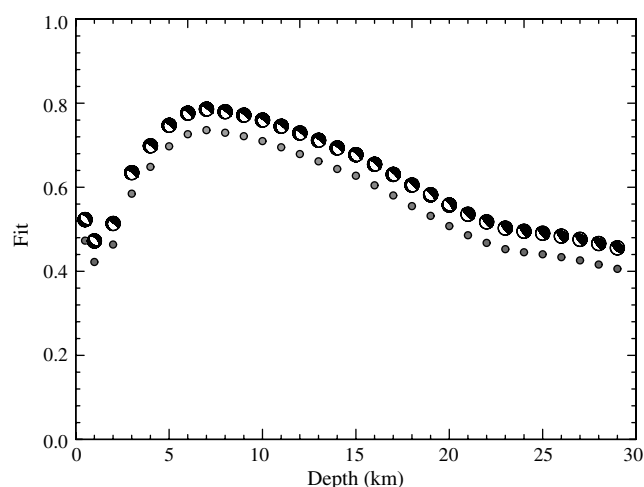
Figure 7. Goodness of fit as a function of source depth for the earthquake of 12 August 2009, 14:51:33. The best-fitting mechanism at each source depth is plotted in a lower hemisphere projection. The best fit is for a depth of 7 km.

Figure 9 compares the observed and predicted waveforms for the station FDMO which is at an epicentral distance of 78.7 km. The observed signal shapes and peak amplitudes are fit well in the synthetics for the best solution in each frequency band. The well-developed surface-wave dispersion that led to the development of the CIA model is obvious. The time shifts indicate that small modifications to make the Rayleigh wave slightly faster and the Love wave slightly slower could be made to the velocity model, but the source solution would not change significantly. The obvious presence of the surface wave, even for this 7 km depth earthquake, has implications for ground-motion scaling at periods as short as 2 s, demanding the use of surface-wave rather than *S*-wave scaling with distance.

Figure 10 summarizes the completeness of the source parameter catalog that we were able to compile. Only for $M_L < 3.3$ is there any significant lack of completeness. Most of the missing small earthquakes occurred within the first day of the aftershock sequence, when their low-frequency content was buried in the incoherent low-frequency coda of the mainshock. Figure 11 compares our moment magnitudes with the automatic network magnitudes, and there is a very good correspondence. However, the moment-tensor inversion depths do not correlate with the automatic depth determination of the network; this is not surprising, given the dependence of depth on the assumed velocity model and on the distribution of the permanent network stations. Chiaraluce *et al.* (2010) recomputed source depths by carefully rereading arrival times and by using a linear gradient velocity model. A comparison of our depths to theirs shows a better correlation. This latter comparison is not sufficient to demonstrate the correctness of our source depths, because we use different velocity models, but we argue that fitting the waveform with a calibrated local velocity model, especially

the large surface wave, provides a much stronger constraint on source depth than using only first-arrival data.

Figure 12 summarizes the source parameters contained in our catalog (Ⓔ see the electronic supplement to this paper). The lower hemisphere focal mechanism plots indicate a normal-faulting environment with the tension axis normal to the trend of the Apennines. Excluding the 11 events that having nodal plane dips $< 25°$ to the southwest, the mean dip is 57° to the southwest with a standard deviation of 13°. Chiaraluce *et al.* (2010) noted that some of the 11 solutions with the shallow dips correlated well with a flattening of hypocenters with depth in the northern part of the study area. We also note, as have others, that the pattern of earthquakes with $M > 3$ shows three groups of hypocenters.

Source inversion was performed independently by the Saint Louis University (SLU) and INGV authors using the same Green's functions and inversion code. The only difference affecting results is the subjective choice of waveforms used for the inversion. Having two catalogs permits an analysis of the variability in the source-parameter estimates, which is summarized in Table 2. This table lists the variability in the source depth, *H*; the moment magnitude; and the strike, dip, and rake angles. Care was taken to compare similarly oriented nodal planes and to reduce the ambiguity of using angles; for example, strikes of 0° and 360° are equivalent as are rakes of $+180°$ and $-180°$. There were more outliers in the strike and dip values than in the *H*, M_w, and dip, but the variability was roughly Gaussian. To avoid any possible bias in the angles and because the earthquakes all represent normal faulting, we also looked at the angles between the *P*-axis vectors for each strike, dip, and rake combination and, similarly, the angles between the *T* axis and the null *B* axis. These angles vary between 0° and 90° and exhibit an approximately Poisson distribution. The entries in this table serve as a guide to confidence in this type of source-parameter estimate. Scognamiglio *et al.* (2010) used the CIA velocity model with a different source inversion code to determine the parameters of all earthquakes with $M_L > 3.5$. A cursory comparison of our moment magnitudes and source depths to theirs indicates that the confidence values in Table 2 are acceptable.

L'Aquila Mainshock

Figure 12 also highlights the fact that the mainshock of the L'Aquila sequence, the earthquake of 6 April 2009, 01:32:39 appears to be shallower than adjacent aftershocks.

We initially had difficulty determining the source parameters of the mainshock. To avoid having to worry about corner frequency effects for a large earthquake, we initially used the 0.01–0.05 Hz frequency band for the inversion, which was the appropriate choice for the 21 February 2008 M_w 5.88 Wells, Nevada, earthquake (see the Data and Resources section). Figure 13 shows the goodness of fit with depth corresponding to this choice; the lack of sensitivity to depth and the tendency toward a large source depth was not
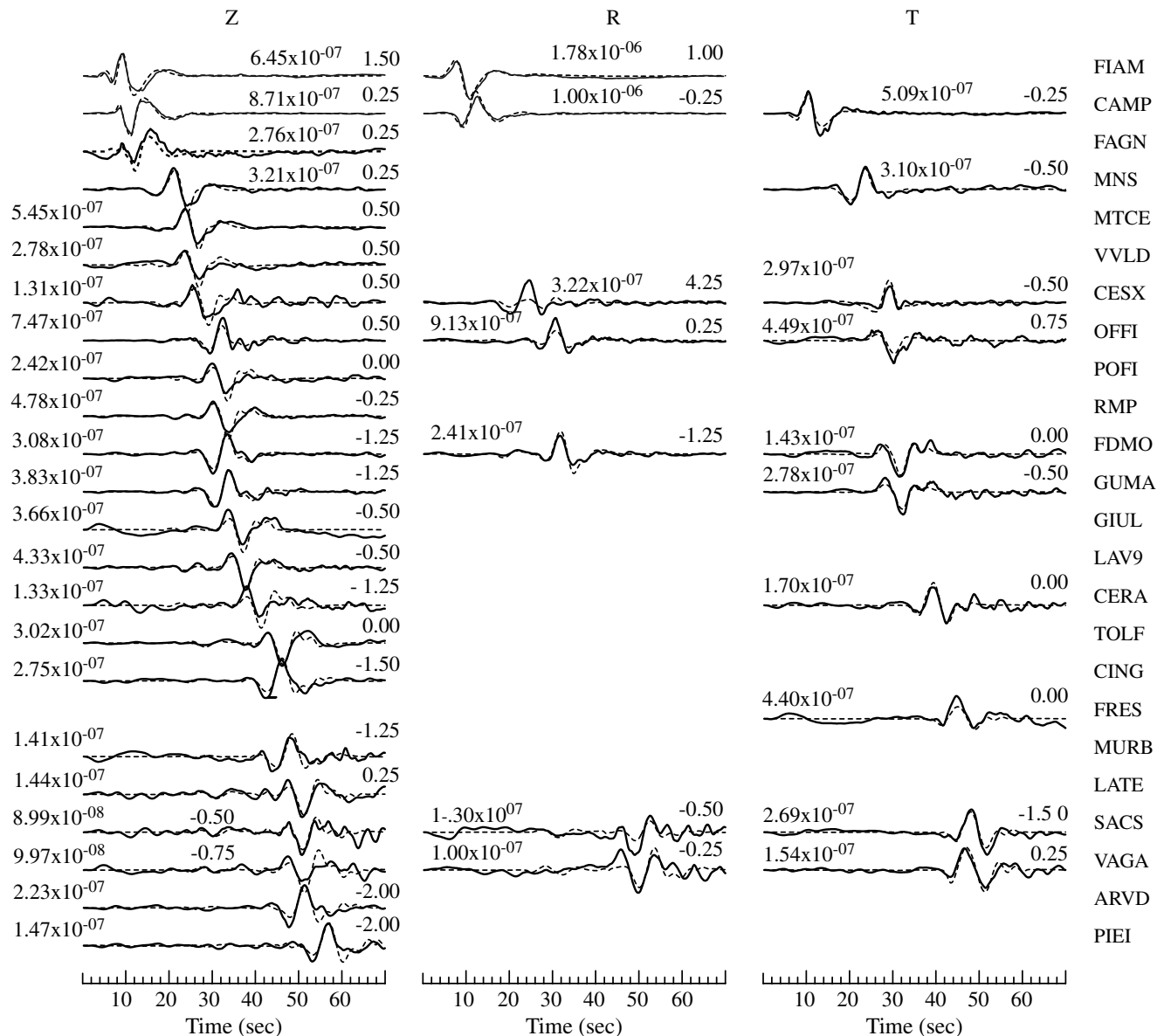
Figure 8. Comparison of observed (solid) and predicted (dashed) waveforms for the earthquake of 12 August 2009, 14:51:33 as a function of absolute travel time. All traces represent ground velocity (m/s) filtered in the 0.02–0.1 Hz band. The peak amplitude is plotted to the left of each trace. The time shift of the synthetic with respect to the observed trace for the best waveform fit is given to the right of each trace. The station name is given to the right of the traces.

satisfying, especially because the source inversions of the aftershocks led to much shallower depths. We then used the 0.01–0.025 Hz frequency band (D. Dreger, personal commun., 2009), which led to Figure 14 and a shallower depth estimate of 5 km. Finally, we added more distant stations (L. Scognamiglio, personal commun., 2009) to reduce sensitivity on nearby, perhaps overdriven sensors on the estimate of the moment magnitude. Figure 15 shows the locations of the stations used for the final broadband inversions and for the sensitivity studies to follow. The epicentral distances vary from 51 to 414 km; seven stations are at distances less than the 146 km used in the model validation study while 13 are at greater distances.

Figure 16 compares the observed and predicted waveforms for the best solution using the 0.01–0.025 Hz passband. The goodness-of-fit parameter was 0.698 when

Table 1
Effect of Frequency Band on Inversion Results of the 12 August 2009, 14:51:33 Earthquake

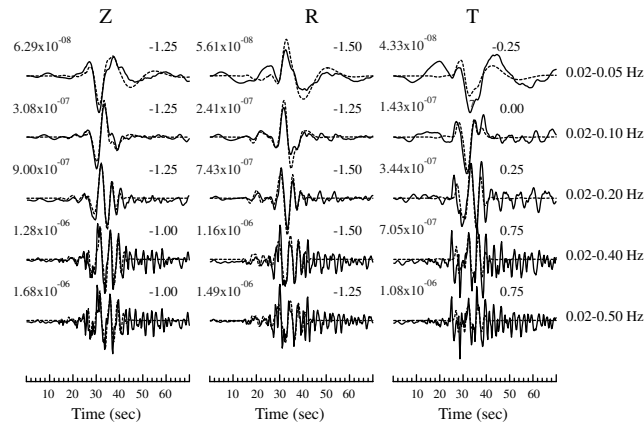| Band (Hz)	H (km)	Strike (°)	Dip (°)	Rake (°)	M_w	Fit
0.02–0.05	9	175	25	−55	3.34	0.47
0.02–0.10	7	185	20	−35	3.34	0.74
0.02–0.20	7	195	20	−25	3.22	0.66
0.02–0.40	7	200	25	−20	3.28	0.31
0.02–0.50	7	200	25	−15	3.27	0.20

Figure 9. Comparison of inversion fits for station FDMO at an epicentral distance of 78.7 km, for different frequency bands used for the inversion. The presentation is the same as that of Figure 8.

using a time window 10 s before and 180 s after the predicted *P*-wave first-arrival time. When using the time window of 0–250 s after origin time, the best fit was 0.695, which is very similar because of the high signal-to-noise ratio. The time shifts in Figure 16 are uniformly positive, but seem to be path-dependent with smaller *Z*-component time shifts to the northwest of the mainshock, perhaps an indication of the need for path-dependent models. The time shifts are much larger than required for the many aftershock solutions.

The requirement for large time shifts to match waveforms can be due to the use of the wrong velocity model for the Green's functions, hypocenter error, or a distributed source process. We discount the model problems for the

Figure 10. Comparison of the number of earthquakes in the catalog and the number of successful moment-tensor solutions as a function of INGV M_L.

stations at short distance because of the validation study of Figure 8. Table 3 is a tabulation of locations available for the mainshock. This tabulation consists of the initial and final locations on ISIDe, our relocations using our *P*-wave first-arrival picks with the Computer Programs in Seismology location code, *elocate* (Herrmann and Ammon, 2004), together with our CIA model, the Michelini *et al.* (2009) relocation that considered two velocity models, and the Chiaraluce *et al.* (2010) location using repicks of all data and a gradient model. Our locations using *elocate* used 24 *P*-wave picks from the broadband stations (BB), 31 *P*-wave picks from the Italian Accelerometric Archive (ITACA ACCEL; see the Data and Resources section), and the combined set of 55 phases. All relocations are moved a few kilometers east with origin times about 1 s later than the initial ISIDe location. Assuming a 2.5–3.0 km/s group velocity for the surface waves, these slight differences in the position of the hypocenter cannot explain the large time delays on the order of 5 s seen in the point-source inversion results in Figure 16. Although the depths are deeper than the 5 km obtained from the point-source inversion, one can argue that the source inversion is sensitive to the centroid of moment release and that the eastern shift of the hypocenter moves the mainshock into a zone of shallower aftershock depths. The use of the CIA model, which has much lower velocities in the upper 1.5 km than even the LI07 model used by Michelini *et al.* (2009), yields the deepest source depth estimate; however, the difference in depth will not significantly affect the surface-wave timing, which makes up the largest part of the signal. We concluded that the source of significant moment release must be shallower and later than the *elocate* solution.

We then decided to apply a simple finite source inversion to fit the regional broadband waveforms by adapting the work of Hartzell and Heaton (1983). We defined a rectangular fault grid, used Green's functions appropriate to the center of each grid cell to the nearest kilometer in epicentral distance and source depth, and let the rupture start at the hypocenter and propagate with a velocity at a fixed fraction of the local *S*-wave velocity obtained from the CIA model. We assumed that the rise-time was fixed at 1.0 s, a value selected to avoid Gibbs' phenomena in the Green's functions, which were computed with a sample interval of 0.25 s. Because the observed waveforms will be modeled in the 0.01–0.025 Hz and 0.01–0.05 Hz bands, the effect of any reasonable subevent rise time will not be resolvable. To permit comparisons with the point-source moment-tensor solutions, the same distance weighting function is applied for the finite-fault inversion and for the final characterization of goodness of fit or reduction of variance. Although we also investigated different rupture initiation points and different rupture velocities, we present the results for just one hypocenter and rupture velocity because our objective is not to provide the definitive mapping of moment release and slip on the fault, but rather to understand both the need for the low-frequency passband and the source of the large time shifts for the point-source solution. The comparisons entail
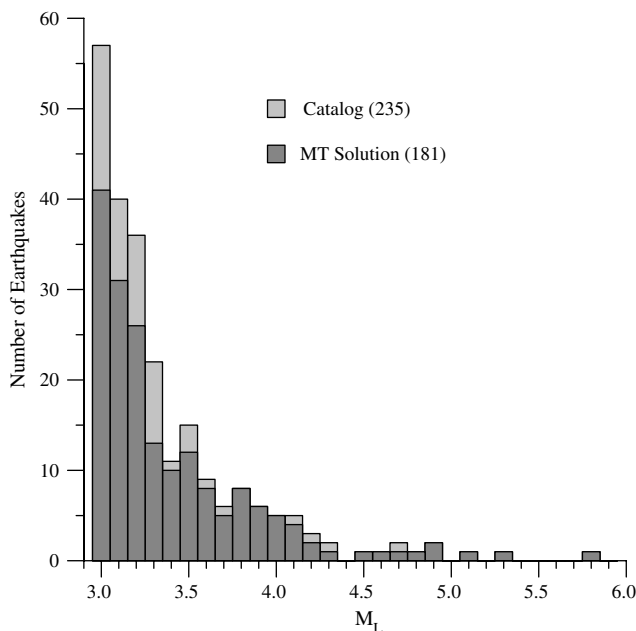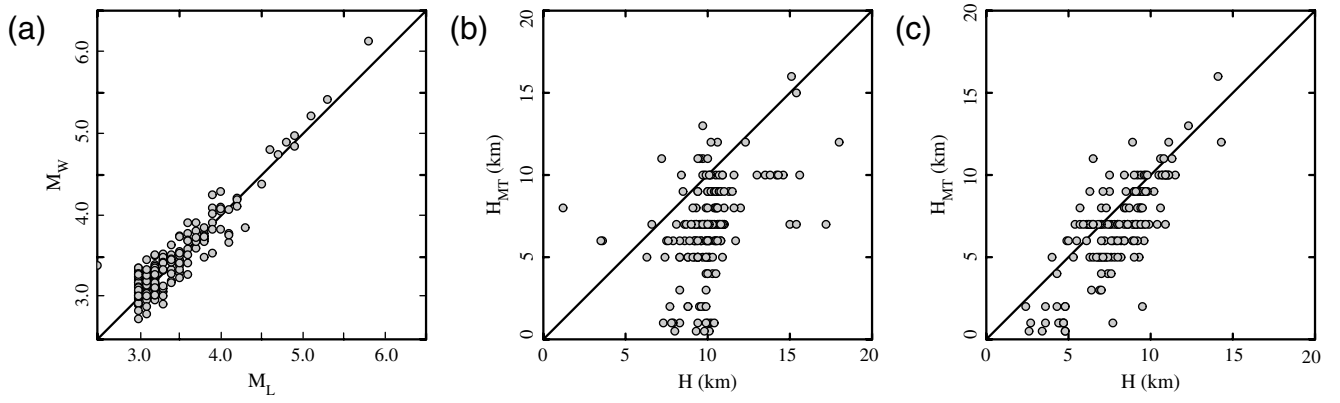
Figure 11. (a) Comparison of M_w from moment-tensor inversion to INGV automatic determination of M_L; (b) Comparison of moment-tensor depths to INGV automatic location depths; (c) Comparison of moment-tensor depths to 1D relocations of Chiaraluce *et al.* (2010).

fitting the 250-s ground-velocity window following the origin time. In all cases, the CIA model is used for the Green's functions.

The fault is characterized by 20 segments of length 2 km along strike, and 25 segments of width 1 km down-dip. The size of the fault plane was chosen to encompass the zone of initial aftershocks, and the hypocenter was centered horizontally in the strike direction. The hypocenter is on the fault at a depth of 13 km at coordinates 42.339° N and 13.371° E, the

fault strikes at 135°, dips at 55°, and has a fixed rake of −95°, which are the parameters determined by the grid search for the mainshock. We chose this nodal plane because the moment-tensor solutions of the aftershocks indicate a trend of increasing depth to the southwest. The total moment release is fixed at M_w 6.13. The system of equations to be solved is

$$[\alpha A, U, \gamma S]^T M = [\alpha d, M_0, 0]^T.$$

Here M is an $n \times 1$ matrix giving the seismic moment release in each of the n cells. A is an $m \times n$ matrix of predicted waveforms for each cell, U is a $1 \times n$ matrix of ones, S is an $n \times n$ Laplacian smoothing matrix, d is a matrix of the waveforms to be fit, and M_0 is the fixed seismic moment. The scaling factor α is selected so that the row norm of A is unity. The factor γ controls the degree of spatial smoothing. Table 4 compares the goodness of fit for the point-source and finite-fault solutions in different passbands as a function of the spatial smoothing factor, the data sets, and the rupture velocity. In the 0.01–0.025 Hz band, the fits are essentially the same, although the finite-fault simulation defines the moment release in cells such that the time-shift problem is addressed. This similarity in fits may be an indication that the point-source solution is adequate in the 0.01–0.025 Hz passband. In the 0.01–0.05 Hz passband, the finite-fault fit is better than for the point-source solution. In the 0.01–0.05 Hz passband, the fit parameters are lower because
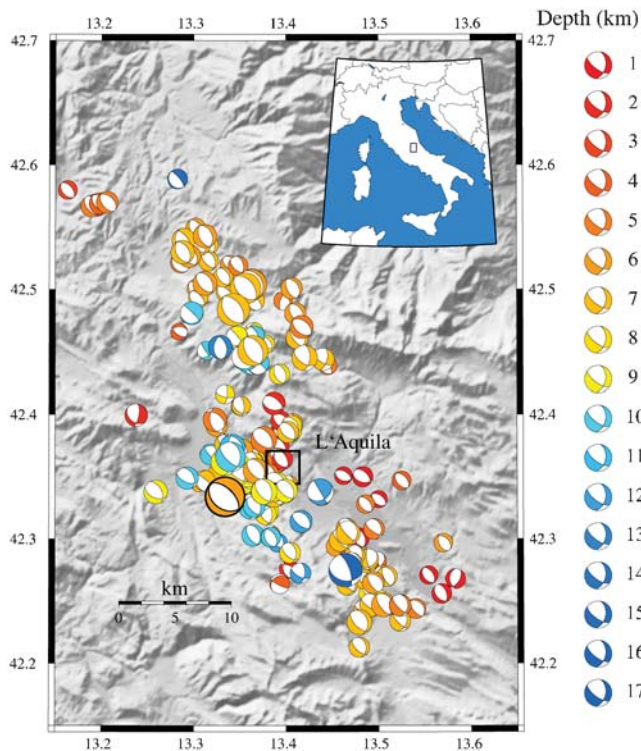

Figure 12. Moment-tensor solutions for the L'Aquila sequence shown in a lower hemisphere equal-area projection. The colors indicate the source depth determined by broadband modeling. Note that the mainshock (largest event) depth is not consistent with the depths of neighboring aftershocks. Subsequent relocations place it about 3 km east, where it is still slightly shallow compared with aftershocks.

Table 2
Source Parameter Variability

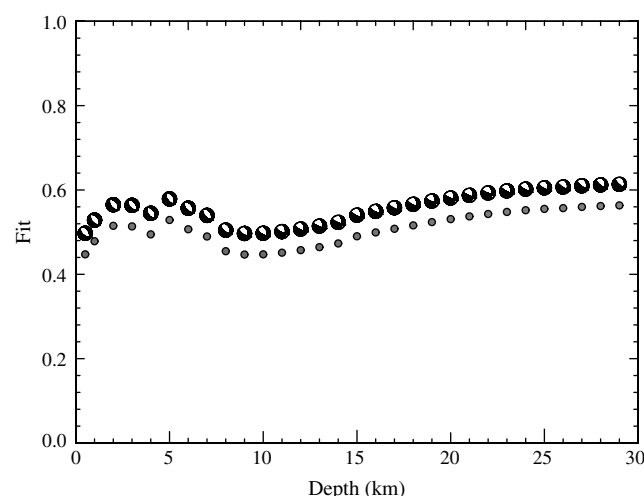| Parameter	Mean	Sigma
H (km)	0	0.9
M_w	0	0.05
Strike (°)	3	10
Dip (°)	−1	7
Rake (°)	1.3	10
Difference in P axis (°)	10	10
Difference in T axis (°)	7	7
Difference in B axis (°)	11	11

Figure 13. Goodness of fit as a function of source depth for the L'Aquila mainshock using the 0.01–0.05 Hz band for inversion. The best fit is at 29 km, the limit of the depth search, although there is a local maximum at a depth of 5 km.

this inversion technique did not permit small time shifts that account for path-dependent propagation differences.

Figure 17 compares observed and predicted waveforms for the 0.01–0.025 Hz passband and the finite-fault parameters of Table 4. The waveforms are well fit in time, except for the surface-wave signal on the transverse component at large distances, indicating the need for a slight refinement in the CIA model. Figure 18 shows the derived discrete finite-fault sources in the 0.01–0.025 Hz passband relative to the locations of the moment tensors that we determined in this study. The hypocenter used for the finite-fault inversion is indicated by the star, and the finite-fault events by the diamonds. The two largest subevents have moment magnitudes of 5.7 and 5.6. Similar plots for inversions in the 0.01–0.05 Hz passband yielded essentially the same pattern.
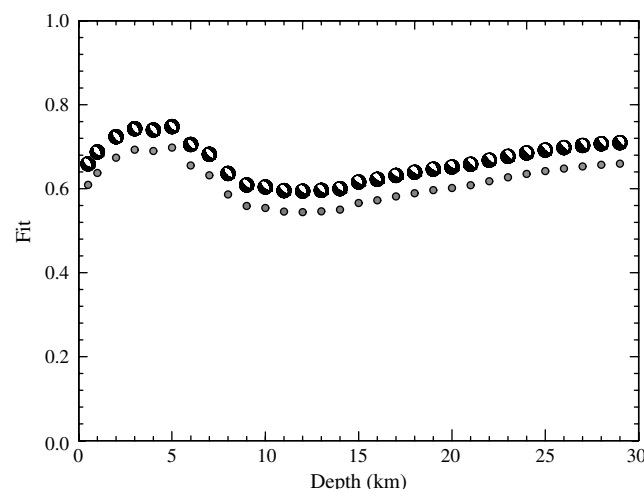

Figure 14. Goodness of fit as a function of source depth for the L'Aquila mainshock using the 0.01–0.025 Hz band for inversion. The best fit is at a depth of 5 km.
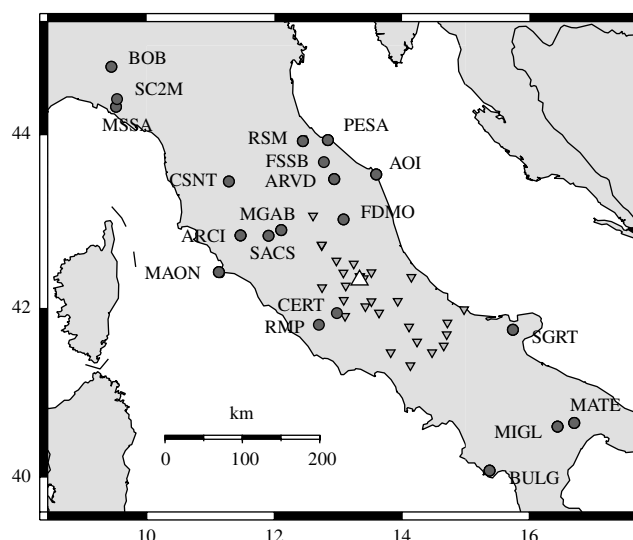

Figure 15. Locations of broadband stations (solid circles) and accelerometers (inverted triangles) used for the analysis of the mainshock (upright triangle).

The facts that the moment release is 3.5–6 s after the assumed origin time and that the subevents are distributed ±10 km along strike with respect to the position of the hypocenter, explain the time shifts required in the point-source solution of Figure 16. We also note that 90% of the moment release is at depths less than 6 km, in agreement with the point-source depth estimate, and that few aftershocks are in the region of major moment release.

Although the solution shown in Figure 18 provides a very good fit to the observed waveforms, it is not realistic in that the corresponding slips are excessive because of the small cell areas. Rather than plotting the seismic moments of the subevents, Figure 19 presents the derived slip, $u = M_0/(\mu A)$, where μ and A are the rigidity and area of each cell, respectively. The figure shows the effect of smoothing, which spreads out the distribution of slip on the fault. The value of the slip has a tendency to be larger at shallower depths because of the smaller rigidities. The common feature of these three inversions is that the fault slip is in the upper 6–7 km and that the time of major slip is delayed 3.5–7 s after the initial break at depth.

Although this numerical exercise accounts for the time shifts required by the point-source solution, the sensitivity of the solution to rupture velocity and the usefulness of the distant broadband data set must be addressed. We combined the ZNE (vertical, north–south, and east–west) component accelerogram data from ITACA, integrated to velocity, with the ZRT (vertical, radial, and transverse) broadband data and inverted the entire data set in the 0.01–0.05 Hz passband, the same passband that could not be used to characterize the mainshock as a point source. The locations of the accelerographs are indicated in Figure 15 by the inverted triangles. Specifically, we added the stations ANT, AQA, AQU, AQV, ASS, AVZ, BOJ, CDS, CHT, CLM, CMB, CMR, CS01,
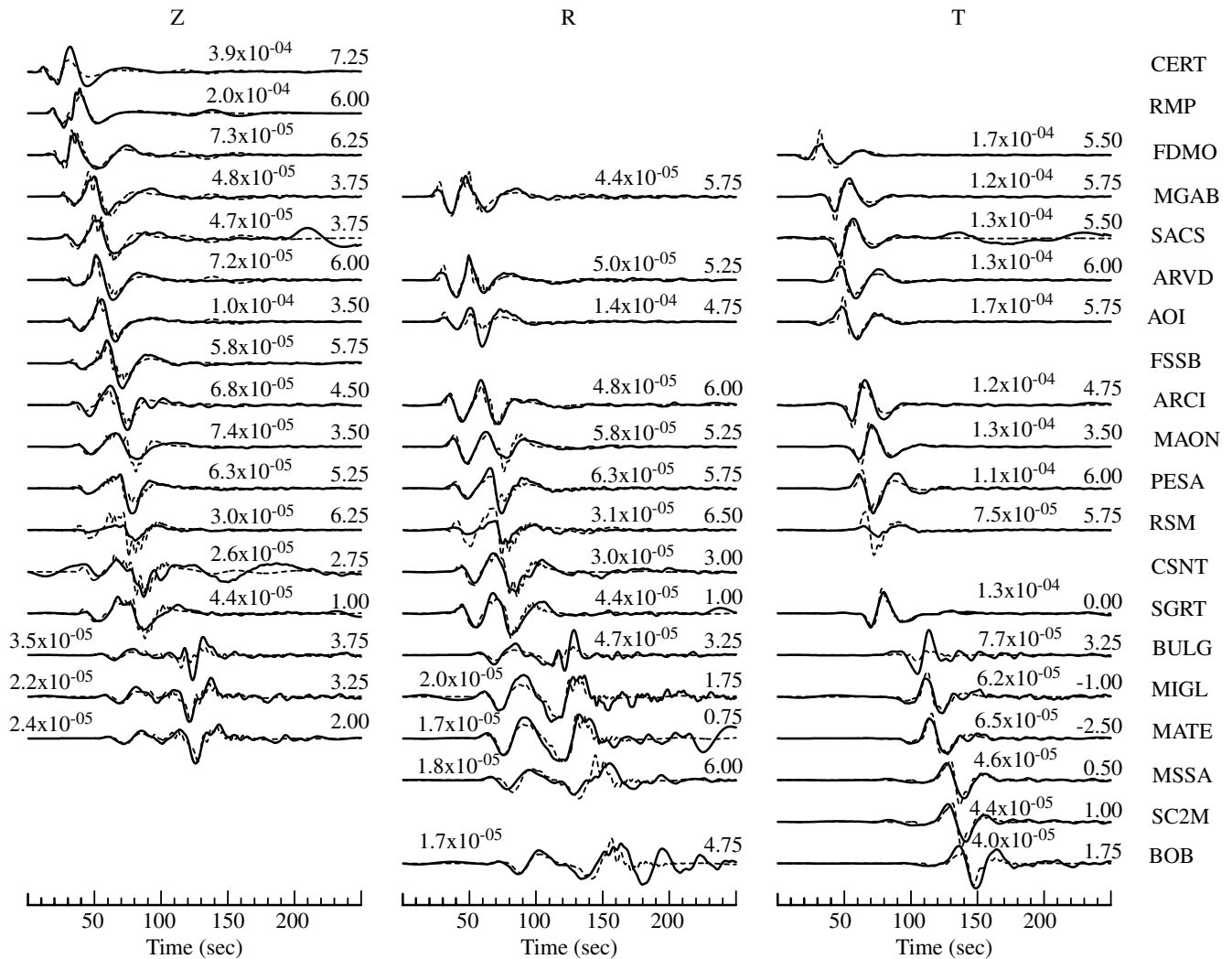
Figure 16. Comparison of observed (solid) and predicted (dashed) waveforms as a function of travel time for the best-fit point-source solution using the 0.01–0.025 Hz frequency band. The figure annotation is as for Figure 8. Note the large positive time shifts of the synthetic with respect to the observed waveform and also the high-frequency motions on parts of the predicted surface-wave arrival.

CSS, FMG, GSA, IRS, LSS, MMP, MTR, ORC, PTF, SBC, SPC, SPO, SUL, TMO, and VRP, which ranged in epicentral distance from about 3 to 140 km. In general, the fits improved with acceleration data included because of the addition of the simpler waveforms at short distances.

Figure 20 shows the derived slip on the fault plane as a function of assumed rupture velocity as a fraction of the local medium S-wave velocity for the two data sets with the smoothing parameter $\gamma = 1$. In order to fit the signal delays seen in Figure 16, the position of maximum slip becomes shallower as the rupture velocity increases because the inversion is in absolute time. We also see that the magnitude of maximum slip increases with increasing rupture velocity because more of the moment release is at shallow depths.

Table 3
Hypocenter Parameters for the L'Aquila Mainshock

Date (yyyy/mm/dd)	Time (UTC)	Latitude (°N)	Longitude (°E)	H (km)	Source
2009/04/06	01:32:39	42.334	13.334	8.8	Initial ISIDe
2009/04/06	01:32:40.4	42.342	13.380	8.3	Final ISIDe
2009/04/06	01:32:39.7	42.341	13.371	13.7	*elocate* BB
2009/04/06	01:32:40.0	42.336	13.369	11.9	*elocate* ACCEL
2009/04/06	01:32:39.8	42.339	13.371	13.3	*elocate* BB + ACCEL
2009/04/06	01:32:40.8	42.347	13.380	9.5	Michelini *et al.*, (2009)
2009/04/06	01:32:40.7	42.350	13.376	9.3	Chiaraluce *et al.* (2010)

Table 4
Comparison of Finite-Fault and Point-Source Inversions

| Inversion	Frequency Band	Fit	Comment
Point source	0.01–0.025	0.700	STK 139; DIP 55; RAKE -94; M_w 6.13; H 5
	0.01–0.05	0.528	STK 138; DIP 56; RAKE -97; M_w 6.03; H 5
Finite-fault	0.01–0.025	0.714	$\gamma = 0.0$ BB; $V_r = V_s$
	0.01–0.05	0.642	$\gamma = 0.0$ BB; $V_r = V_s$
	0.01–0.05	0.610	$\gamma = 0.0$ BB; $V_r = 0.8 V_s$
	0.01–0.05	0.542	$\gamma = 0.0$ BB; $V_r = 0.6 V_s$
	0.01–0.05	0.654	$\gamma = 0.0$ BB + ACCEL; $V_r = V_s$
	0.01–0.05	0.648	$\gamma = 0.0$ BB + ACCEL; $V_r = 0.8 V_s$
	0.01–0.05	0.569	$\gamma = 0.0$ BB + ACCEL; $V_r = 0.6 V_s$
	0.01–0.05	0.646	$\gamma = 0.1$ BB + ACCEL; $V_r = V_s$
	0.01–0.05	0.643	$\gamma = 0.1$ BB + ACCEL; $V_r = 0.8 V_s$
	0.01–0.05	0.553	$\gamma = 0.1$ BB + ACCEL; $V_r = 0.6 V_s$
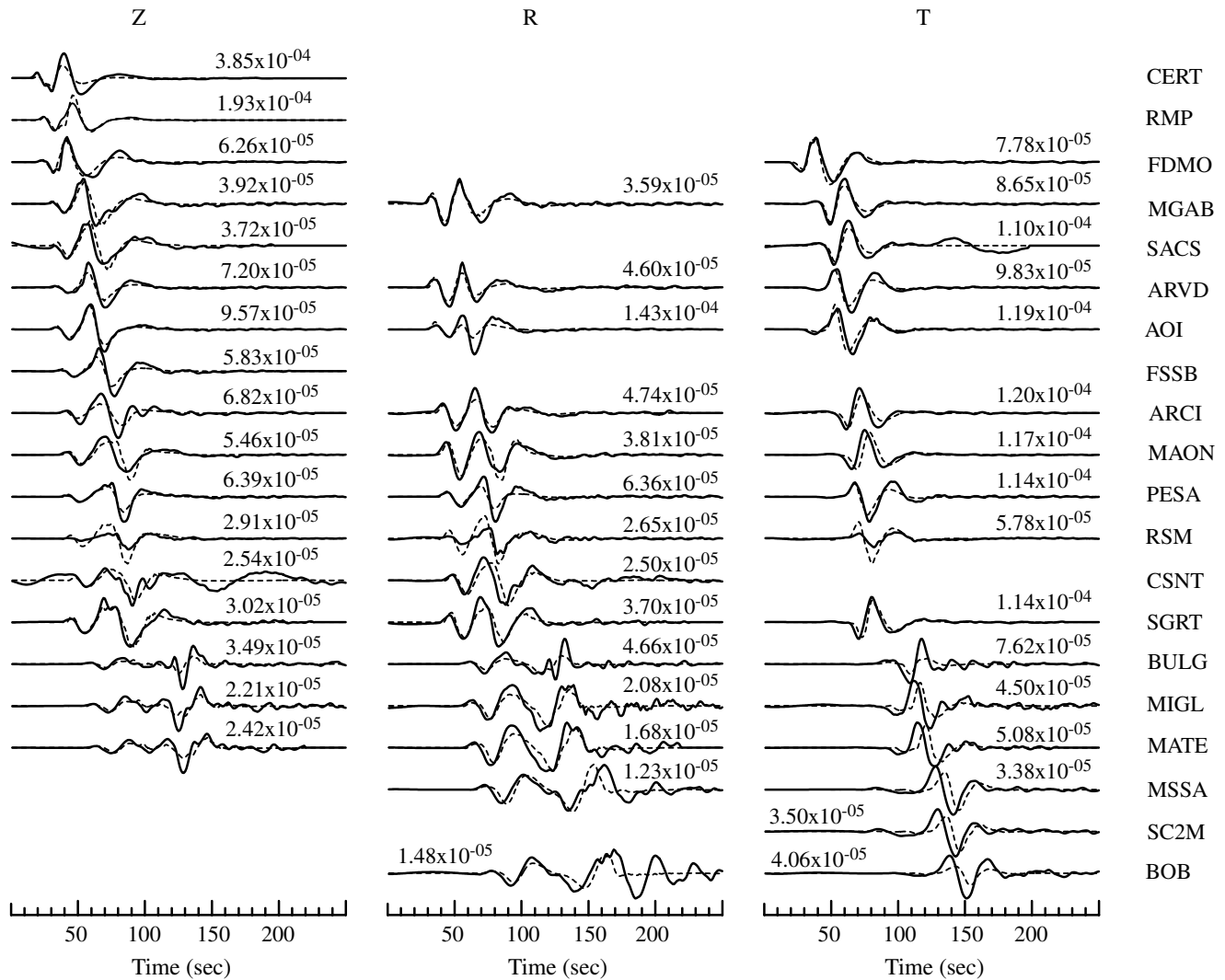
Figure 17. Comparison of finite-fault waveforms (dashed) to observed ground velocities (solid) in the 0.01–0.025 Hz band. No spatial smoothing is assumed, and rupture velocity equals the local *S*-wave velocity. The misalignment in the surface-wave arrival at larger distances indicates the need for slight changes in the velocity model.
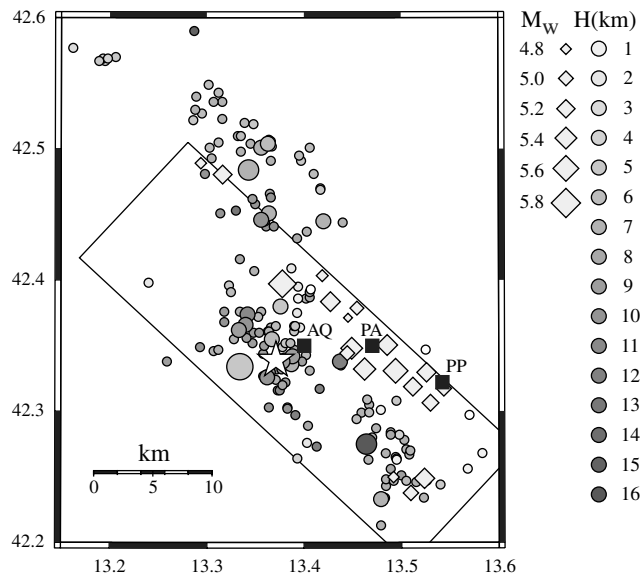
Figure 18. Location of finite-fault subevents with respect to our moment-tensor solutions. Shaded circles: events for which moment-tensor inversions were determined in this study with the shading a function of source depth; the largest circle is the location of the initial automatic solution for the mainshock. Star: initiation point for finite-fault rupture. Diamonds: finite-fault subevents. Small squares indicate nearby cities. AQ, L'Aquila; PA, Paganica; and PP, Poggio Picenze. The size of all events is scaled with magnitude.

The shapes and locations of the major slip are similar for both waveform data sets.

Figure 21 decreases the smoothing parameter to $\gamma = 0.1$, with the consequence that more character is seen in the slip distributions. Again there is similarity in the patterns derived from the two data sets for the same rupture velocity parameter. However, the addition of acceleration data sharpens the slip pattern. The goodness of fit associated with these inversions are all better than that of the point-source solution for the 0.01–0.05 Hz frequency band.

Discussion

This study was able to provide a very complete moment-tensor catalog of 181 earthquakes down to M_w 3 for the L'Aquila earthquake sequence for several reasons: the INGV has a dense broadband digital seismic network in the epicentral region, the earthquakes occurred at the time of year when microseismic noise started to decrease, the earthquakes generated high amplitude dispersed surface waves because of the local velocity structure at shallow depths, and finally, the aftershock sequence was very energetic in terms of the numbers of aftershocks with $M_w \geq 3.0$. Normal faulting with almost all tension axes in the east to east–northeast directions characterizes the solutions.

Our catalog of regional moment-tensor solutions differs very little from that developed by Scognamiglio et al. (2010) because both use the same CIA velocity model and similar
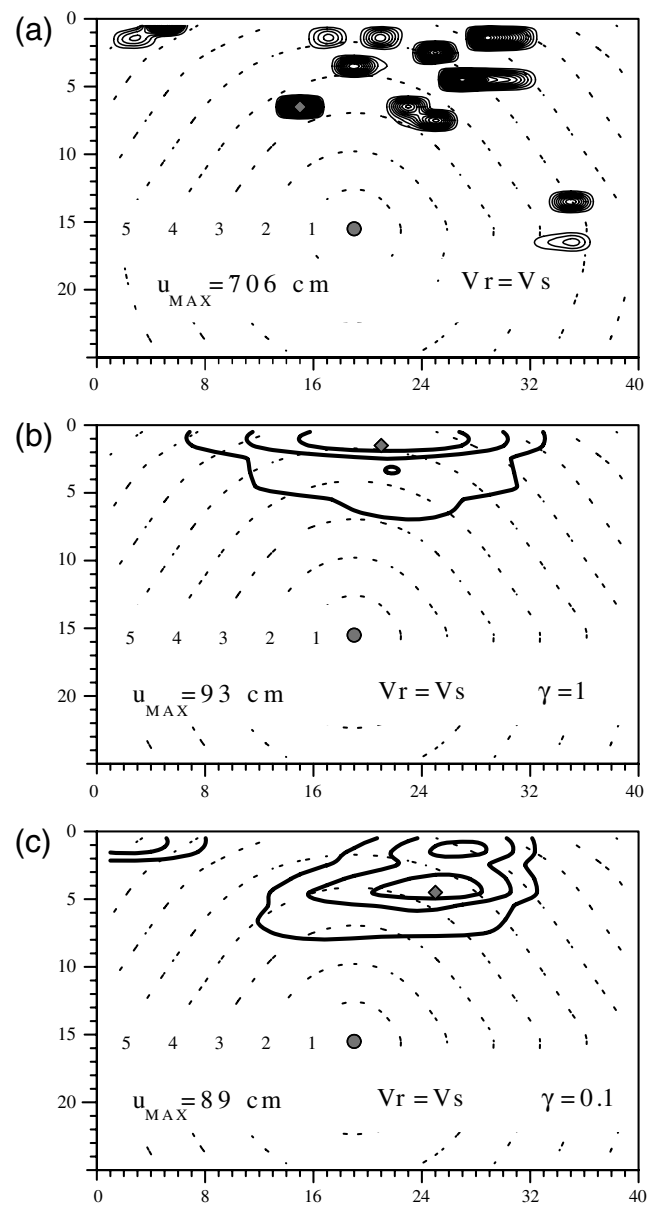

Figure 19. Sensitivity of finite-fault inversion of broadband data in the 0.01–0.025 Hz band to smoothing for a fixed rupture velocity equal to local S-wave velocity. (a) smoothing parameter = 0.0, (b) smoothing parameter = 1.0, and (c) smoothing parameter = 0.1. The rupture velocity was set to the local shear-wave velocity. The solid circle indicates the hypocenter, and the diamond the point of maximum slip. The dashed gray lines indicate the rupture timing in seconds. The slip contours increase from 25 to 700 cm with the same shading for all images.

filtered ground velocity waveforms. Details of the small differences in the two catalogs are given in the paper by Scognamiglio et al. (2010). Their effort, though, focused on earthquakes with $M_w \geq 3.5$ and on automatic processing. A comparison of 25 regional centroid moment-tensor solutions determined by Pondrelli et al. (2010) for the larger earthquakes showed that our moment magnitudes were smaller by $0.22 M_w$ units and our depths were shallower by 5 km
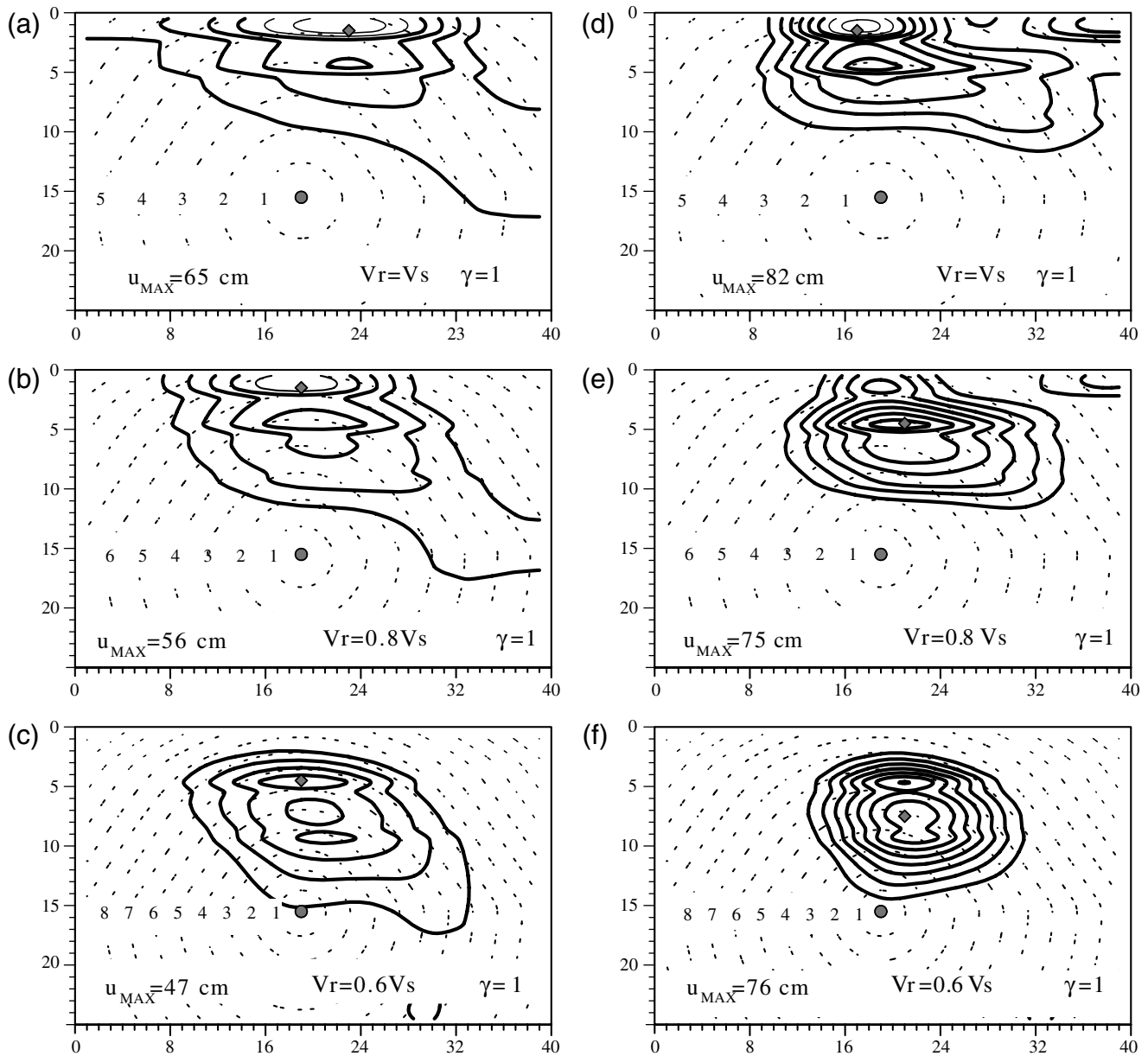
Figure 20. Sensitivity of finite-fault inversion of broadband data in the 0.01–0.05 Hz band to rupture velocity. A fixed smoothing parameter of 1.0 is used. The left-column data set (a–c) consists of only the regional broadband data, while the right-column data set (d–f) adds local acceleration records. Rupture velocity decreases as a function of the shear-wave velocity from top to bottom as 1.0, 0.8, and 0.6. The solid circle indicates the hypocenter, and the diamond the location of maximum slip. The dashed gray lines indicate the rupture timing in seconds. The slip contours increase from 25 to 700 cm with the same shading for all images.

than theirs. We attribute this difference to our use of waveform data within 200–300 km to the exclusion of any paths through the sea, the use of high frequencies and, more importantly, a crustal model calibrated for the propagation paths used. In simple terms, the moment magnitude value is not independent of the velocity model used, which must be presented alongside the M_ws.

We found that the determination of the source parameters of the mainshock required much care in the selection of the frequency band and data sets for inversion. Although

we initially assumed that the 0.01–0.05 Hz band would be adequate, given previous experience with the similar-sized 2008 Wells, Nevada, normal-faulting event, the grid-search solution diverged to depths deeper than expected for the source region. The use of the lower 0.01–0.025 Hz passband, at the suggestion of D. Dreger (personal commun., 2008), alleviated the problem, but the goodness of fit did not show as well-defined sensitivity to depth as seen in the application of the same procedures to the smaller aftershocks (e.g., Fig. 7). We are not sure how much of this problem arises
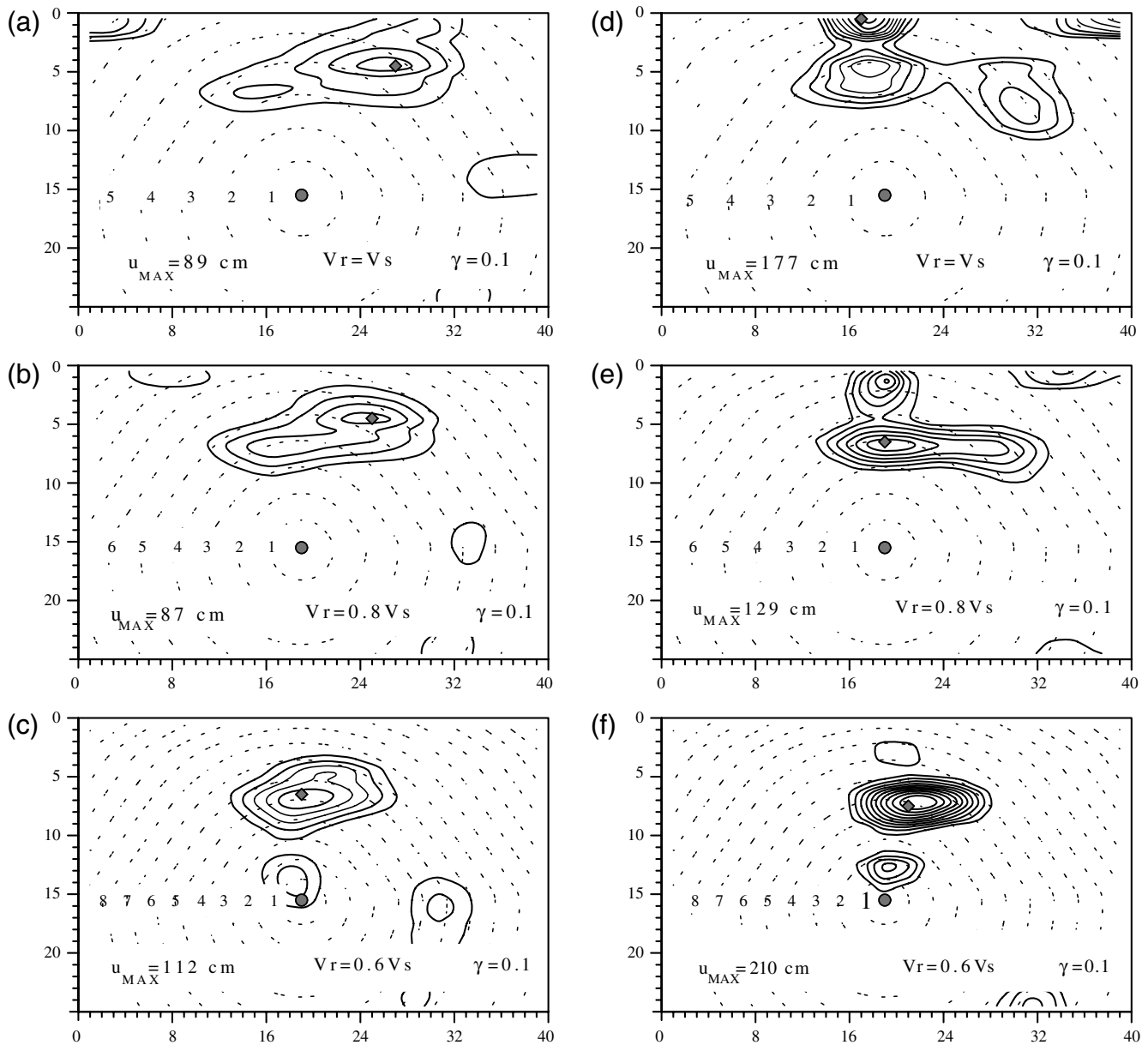
Figure 21. Sensitivity of finite-fault inversion of broadband data in the 0.01–0.05 Hz band to rupture velocity. A fixed smoothing parameter of 0.1 is used. The left-column data set (a–c) consists of only the regional broadband data, while the right-column data set (d–f) adds local acceleration records. Rupture velocity decreases as a function of the shear-wave velocity from top to bottom as 1.0, 0.8, and 0.6. The solid circle indicates the hypocenter, and the diamond the location of maximum slip. The dashed gray lines indicate the rupture timing in seconds. The slip contours increase from 25 to 700 cm with the same shading for all images.

from the nonuniform station distribution in azimuth because of the geometry of the Italian peninsula or because of the lack of data at short distances because of overdriven sensors. From experience in inverting surface-wave spectral amplitudes (R. B. Herrmann, unpublished manuscript, 2010), we know that the effect of increasing depth is to reduce the high frequency content of the fundamental mode surface waves (Tsai and Aki, 1971). This effect must also be apparent in the time domain if the surface wave is the dominant part of the observed signal. Our finite-fault inversions yielded a sequence of shallow events distributed in time and space, which have the effect of modifying the higher-frequency content of the observed signal due to signal interference at high frequencies, when compared with that of a point source. The point-source inversion interprets this effect as an increased source depth. The important lesson learned is that if the goodness of fit, as seen in Figure 13, is observed in a region where one expects upper crustal earthquakes, then one should invert the data again using a lower passband and also consider the source to be spatially complex.

A second indication of a spatially complex source is the fact that large time shifts were required to match observed waveform data, even when using the lower-frequency band. We investigated the effect of different data sets and velocity models, and concluded that the epicenter was not very sensitive to the velocity model or location technique and that the differences in origin time were not sufficient to explain the required time shifts in the inversion of the regional broadband data sets. We concluded that the centroid of moment release was not the hypocenter based on first arrivals. This simple finite-source inversion demonstrated the ability to fit the regional waveforms in absolute time because of the use of a calibrated regional velocity model.

Our finite-fault modeling of regional broadband waveforms requires that the major moment/slip release occur roughly 4–7 s after the origin time and up-dip of the hypocenter. The use of regional and local data sets in the 0.01–0.05 Hz passband cannot resolve issues of the choice of rupture velocity and degree of spatial smoothing, other than that smoothing is required to avoid extreme values of slip and that the distance of the major fault slip is a function of the rupture velocity. We also note that the goodness-of-fit parameter cannot be used as the sole criteria for defining the solution, because, as we have seen, physically unrealistic answers of large slip may result. The resolution of these questions cannot be accomplished without other data, such as measurements of permanent deformation near the fault from integrated accelerograms, GPS, or InSar, or perhaps from broadband modeling of teleseismic data that will be sensitive to the depth of the slip release.

The shallow depth of major slip is comparable to that estimated by Atzori *et al.* (2009) from an inversion of DInSar data. It is also interesting that there are few significant (e.g., $M_L > 3$) aftershocks associated with the unsmoothed inversion of low-frequency data shown in Figure 18. Neither the Atzori *et al.* (2009) nor any of our solutions are compatible with the inversion of GPS and strong-motion data by Cirella *et al.* (2009), who have the major slip at about 42.28° N and 13.43° E, near the location of the large, deep aftershock seen in Figure 18. However, a reevaluation of the inversion of GPS and strong-motion data using the CIA velocity model developed in this paper (Scognamiglio *et al.*, 2010) has major slip up-dip from the hypocenter with directivity to the southeast.

The inversion of just the broadband data did serve to highlight the spatial location of the shallow moment and slip release in a manner that overcame the initial bias due to the first-motion hypocenter by moving the large fault motion up-dip from about 13 km to 5 km deep, a significant change in terms of expected surface motions.

The L'Aquila mainshock is interesting for another reason. What is the significance of the initial hypocenter to the main moment release? If our finite-fault solution that fits regional waveforms in travel time is reasonable, is the initial event at depth the trigger for the large earthquake,

or is it just coincidental? The first option seems more reasonable from the point of view of modeling the regional broadband waveforms because it is hard to conceive of a near-instantaneous rupture process that propagates horizontally, while the shear waves from a trigger earthquake at depth might reach the shallow slip regions in the appropriate sequence.

This study provides a unique compilation of waveform-constrained source parameters for over 180 aftershocks. The depths and source mechanisms are constrained well by the data sets and have already been used in the interpretation of the dynamics of the sequence and the identification of fault structures that were activated by the changes in stress during this sequence.

Because of our success in deriving source parameters for small events, we have extended the application of our inversion technique to the entire peninsula, not only because of curiosity about the source process but also as a test of the spatial limits on the applicability of our regional crustal model. Having one or more regional velocity models with precomputed Green's functions available is an essential part of being able to automate the moment-tensor determination in order to be prepared for the next large earthquake in Italy.

Data and Resources

Some figures were created using the GMT package of Wessel and Smith (1991). Broadband waveform data from the Italian Instrumental and Parametric Data-Base (ISIDe) is available at http://iside.rm.ingv.it/iside/standard/index.jsp (last accessed October 2010).

The strong-motion data from the Italian Accelerometric Archive (ITACA) is available at http://itaca.mi.ingv.it/ItacaNet/ (last accessed October 2010).

Computer Programs in Seismology is available at http://www.eas.slu.edu/Earthquake_Center/CPS/CPS330.html (last accessed October 2010). The Istituto Nazionale di Geofisica e Vulcanologia web site is http://www.ingv.it.

A record of the processing steps listed in the Moment-Tensor Solutions section can be viewed at http://www.eas.slu.edu/Earthquake_Center/MECH.IT/. For more information on the Wells, Nevada, earthquake, see http://www.eas.slu.edu/Earthquake_Center/MECH.NA/20080221141605/.

References

Akinci, A., and L. Malagnini (2009). The 2009 Abruzzo earthquake, Italy, *IRIS Newsletter*, rept. no. 1.

Akinci, A., F. Galadini, D. Pantosti, M. Petersen, L. Malagnini, and D. Perkins (2009). Effect of time dependence on probabilistic seismic-hazard maps and deaggregation for the central Apennines, Italy, *Bull. Seismol. Soc. Am.* **99,** no. 2A, 585–610, doi 10.1785/0120080053.

Akinci, A., L. Malagnini, and F. Sabetta (2010). Characteristics of the strong ground motions from the 6 April 2009 L'Aquila earthquake, Italy, *Soil Dynam. Earthq. Eng.* **30,** 320–335, doi 10.1016/j.soil-dyn.2009.12.006.

Amato, A., and F. Mele (2008). Performance of the UNGV National Seismic Network from 1997 to 2007, *Ann. Geophys.* **51,** 417–431.

Anzidei, M., E. Boschi, V. Cannelli, R. Devoti, A. Esposito, A. Galvani, D. Melini, G. Pietrantonio, F. Riguzzi, V. Sepe, and E. Serpelloni (2009). Coseismic deformation of the destructive April 6, 2009 L'Aquila earthquake (central Italy) from GPS data, *Geophys. Res. Lett.* **36,** L17307, doi 10.1029/2009GL039145.

Atzori, S., I. Hunstad, M. Chini, S. Salvi, C. Tolomei, C. Bignami, S. Stramondo, E. Trasetti, A. Antonioli, and E. Boschi (2009). Finite fault inversion of DinSAR coseismic displacement of the 2009 L'Aquila earthquake (central Italy), *Geophys. Res. Lett.* **36,** L15305, doi 10.1029/2009GL039293.

Bagh, S., L. Chiaraluce, P. De Gori, M. Moretti, A. Govoni, C. Chiarabba, P. Di Bartolomeo, and M. Romanelli (2007). Background seismicity in the central Apennines of Italy: The Abruzzo region case study, *Tectonophysics* **444,** 80–92, doi 10.1016/j.tecto.2007.08.009.

Boncio, P., G. Lavecchia, G. Milana, and B. Rozzi (2004). Improving the knowledge on the seismogenesis of the Amatrice–Campotosto area (central Italy) through an integrated analysis of minor earthquake sequences and structural data, *Ann. Geophys.* **47,** 1723–1742.

Chiarabba, C., L. Jovane, and R. DiStefano (2005). A new look to the Italian seismicity: Seismotectonic inference, *Tectonophysics* **395,** 251–268 doi 10.1016/j.tecto.2004.09.013.

Chiaraluce, L., C. Chiarabba, P. De Gori, R. Di Stefano, L. Improta, D. Piccinini, A. Schlagenhauf, P. Traversa, L. Valoroso, and C. Voisin (2010). The April 2009 L'Aquila (central Italy) seismic sequence, *Bull. Theor. Appl. Geophys.*, available at http://www.earth-prints.org/handle/2122/6487.

Cirella, A., A. Piatanesi, M. Cocco, E. Tinti, L. Scognamiglio, A. Michelini, A. Lomax, and E. Boschi (2009). Rupture history of the 2009 L'Aquila (Italy) earthquake from non-linear joint inversion of strong motion and GPS data, *Geophys. Res. Lett.* **36,** L19304, doi 10.1029/2009GL039795.

De Luca, G., R. Scarpa, L. Filippi, A. Gorini, S. Marcucci, P. Marsan, G. Milana, and E. Zambonelli (2000). A detailed analysis of two seismic sequences in Abruzzo, central Apennines, Italy, *J. Seismol.* **4,** 1–21.

Di Luzio, E., G. Mele, M. M. Tiberti, G. P. Cavinato, and M. Parotto (2009). Moho deepening and shallow upper crustal delamination beneath the central Apennines, *Earth. Planet. Sci. Lett.* **280,** 1–12, doi 10.1016/j.epsl.2008.09.018.

Emergeo Working Group (2009). Rilievi geologici di terreno effettuati nell'area epicentrale della sequenza sismica dell'Aquilano del 6 aprile 2009, report, Ist. Naz. Geofis. Vulcanol., Rome, available at http://www.earth-prints.org/handle/2122/5036 (in Italian).

Hartzell, S. H., and T. H. Heaton (1983). Inversion of strong ground motion and teleseismic waveform data for the fault rupture history of the 1979 Imperial Valley, California, earthquake, *Bull. Seismol. Soc. Am.* **73,** 1553–1583.

Herrmann, R. B. (1973). Some aspects of band-pass filtering of surface waves, *Bull. Seismol. Soc. Am.* **63,** 703–711.

Herrmann, R. B., and C. J. Ammon (2002). Computer programs in seismology—3.30: Surface waves, receiver functions and crustal structure, www.eas.slu.edu/People/RBHerrmann/CPS330.html.

Herrmann, R. B., and C. J. Ammon (2004). Computer programs in seismology—3.30: GSAC—Generic seismic application coding, www.eas.slu.edu/People/RBHerrmann/CPS330.html.

Hunstad, I., G. Selvaggi, N. D'Agostino, P. England, P. Clarke, and M. Pierozzi (2003). Geodetic strain in peninsular Italy between 1875 and 2001, *Geophys. Res. Lett.* **30,** no. 4, doi 10.1029/2002GL016447.

Lavecchia, G., F. Brozzetti, M. Barchi, J. Keller, and M. Meinichetti (1994). Seismotectonic zoning in east-Central Italy deduced from the analysis of the Neogene to present deformations and related stress fields, *Geol. Soc. Am. Bull.* **106,** 1107–1120.

Ligorria, J. P., and C. J. Ammon (1999). Iterative deconvolution and receiver-function estimation, *Bull. Seismol. Soc. Am.* **89,** 1395–1400.

Mariucci, M. T., A. Amato, and P. Montone (1999). Recent tectonic evolution and present stress in the northern Apennines (Italy), *Tectonics* **18,** 108–118, doi 10.1029/1998TC900019.

Massonnet, D., M. Rossi, C. Carmona, F. Adragna, G. Peltzer, K. Feigl, and T. Rabaute (1993). The displacement field of the Landers earthquake mapped by radar interferometry, *Nature* **364,** 138–142.

Michelini, A., L. Faenza, V. Lauciani, and L. Malagnini (2008). ShakeMap implementation in Italy, *Seismol. Res. Lett.* **79,** 5, doi 10.1785/gssrl.79.5.688.

Michelini, A., L. Faenza, A. Lomax, and M. Cocco 92 (2009). Appraisal of the hypocentral location of the L'Aquila main shock, *Eos Trans. AGU* **90,** no. 52, Fall. Meet. Suppl., Abstract U23A-0027.

Montone, P., M. T. Mariucci, S. Pondrelli, and A. Amato (2004). An improved stress map for Italy and surrounding regions (central Mediterranean), *J. Geophys. Res. B Solid Earth Planets* **109,** B10410. doi 10.1029/2003JB002703.

Pace, B., L. Peruzza, G. Lavecchia, and P. Boncio (2006). Layered seismogenic source model and probabilistic seismic-hazard analyses in Central Italy, *Bull. Seismol. Soc. Am.* **96,** no. 1, 107–132, doi 10.1785/0120040231.

Pondrelli, S., S. Salimbeni, A. Morelli, G. Ekström, M. Olivieri, and E. Boschi (2010). Seismic moment tensors of the April 2009, L'Aquila (Central Italy) earthquake sequence, *Geophys. J. Int.* **180,** 238–242.

Scognamiglio, L., E. Tinti, and A. Michelini (2009). Real-time determination of seismic moment tensor for the Italian region, *Bull. Seismol. Soc. Am.* **99,** 2223–2342.

Scognamiglio, L., E. Tinti, A. Michelini, D. Dreger, A. Cirella, M. Cocco, S. Mazza, and A. Piatanesi (2010). Fast determination of moment tensors and rupture history: Application to the April 6th 2009, L'Aquila earthquake, *Seismol. Res. Lett.* **8,** 892–906.

Scrocca, D., C. Doglioni, P. Innocenti, A. Manetti, L. Mazzotti, L. Bertelli, L. Burbi, and S. D'Offizi (2003). CROP Atlas: Deep seismic reflection profile of the Italian crust, *Mem. Descr. Carta Geol. Ital.*, 62.

Selvaggi, G., B. Castello, and R. Azzara (1997). Spatial distribution of scalar seismic moment release in Italy (1983–1996): Seismotectonic implications for the Apennines, *Ann. Geophys.* **40,** no. 6, 1565–1578.

Stucchi, M., R. Camassi, A. Rovida, M. Locati, E. Ercolani, C. Meletti, P. Migliavacca, F. Bernardini, and R. Azzaro (2007). DBMI04, il database delle osservazioni macrosismiche dei terremoti Italiani utilizzate per la compilazione del catalogo parametrico CPTI04, *Quaderni Geofisic.* **49,** 38 (in Italian).

Tsai, Y., and K. Aki (1971). Amplitude spectra of surface waves from small earthquakes and underground nuclear explosions, *J. Geophys. Res.* **76,** 3940–3952.

Walters, R. J., J. R. Elliot, N. D'Agostino, P. C. England, I. Hunstad, J. A. Jackson, B. Parsons, R. J. Phillips, and G. Roberts (2009). The 2009 L'Aquila earthquake (central Italy): A source mechanism and implications for seismic hazard, *Geophys. Res. Lett.* **36,** L173312, doi 10.1029/2009GL039337.

Wessel, P., and W. Smith (1991). Free software helps map and display data, *Eos Trans. AGU* **72,** 441, 445–446.

Westaway, R. (1992). Revised nucleation point and fault rupture geometry for the 1980 Campania-Basilicata earthquake in southern Italy, *Geophys. J. Int.* **109,** 376–390.

Appendix

Table A1
Velocity Models

H (km)	V_P (km/s)	V_S (km/s)	Density (kg/m^3)
Initial Model			
1.5	5.0	2.86	2515
3	6.0	3.43	2687
3	6.0	3.43	2687
7	6.3	3.57	2754
15	6.0	3.43	2687
6	6.7	3.78	2850
8	7.1	3.99	2956
–	7.9	4.40	3212
CIA (Surface Wave)			
1.5	3.75	2.14	2275
3	4.94	2.82	2485
3	6.01	3.43	2706
7	5.55	3.15	2609
15	5.88	3.36	2677
6	7.11	4.01	3010
8	7.10	3.99	3012
–	7.90	4.40	3276
ACI (Surface Wave and Receiver Function)			
0.5	4.03	2.30	2323
0.5	3.81	2.18	2287
0.5	3.73	2.13	2271
1	4.54	2.59	2398
1	5.16	2.95	2532
1	5.58	3.18	2616
3	5.69	3.25	2637
3	5.38	3.05	2576
4	6.05	3.43	2714
5	5.51	3.15	2602
5	6.16	3.52	2747
5	5.76	3.29	2651
6	6.42	3.62	2828
8	7.35	4.13	3090
–	7.90	4.40	3276

Department of Earth and Atmospheric Sciences of
Saint Louis University
3642 Lindell Boulevard
St. Louis, Missouri 63108
rbh@eas.slu.edu
    (R.B.H.)

Istituto Nazionale di Geofisica e Vulcanologia
Via di Vigna Murata 605
00143 Rome, Italy
    (L.M., I.M.)